

Mesoscopic hydrodynamics of diphasic Lattice Bhatnagar Gross Krook fluid interfaces

S. P. Thompson,^a I. Halliday^b and C. M. Care^c

^a Computer Services for Academic Research (CSAR), Manchester Computing, The University of Manchester, Oxford Road, Manchester, UK M13 9PL

^b Division of Applied Physics, School of Science and Mathematics, Sheffield Hallam University, Pond Street, Sheffield, UK S1 1WB

^c Materials Research Institute, Sheffield Hallam University, Pond Street, Sheffield, UK S1 1WB

Received 16th December 1998, Accepted 19th February 1999

We consider the most appropriate way to assess the interfacial tension locally, on a meso-scale, in one particular class of diphasic lattice Bhatnagar Gross Krook fluid, in which the interface is supported by a simple segregation algorithm. Our investigative methodology and observations will support similar analysis of other lattice Boltzmann models containing discrete interfaces. By assessing the performance of a lattice fluid/fluid interface against the most general hydrodynamic boundary conditions, we measure an orientational dependence in the model's surface tension. In attempting to assess this anisotropy, which must obstruct the performance of the model and others similarly conceived, we devise a simple correction to the segregation algorithm. The useful result provides a platform for future work.

1 Introduction

Given their physical and practical significance, it is unfortunate that traditional numerical methods find difficulty in simulating *diphasic* fluids: two-component immiscible fluid mixtures. The past decade has, however, seen increasing interest in the study of rheological problems using better-adapted, novel techniques. Lattice Boltzmann (LB) simulation is one such method with acknowledged advantages making LB a very useful tool for simulating (amongst other things) diphasic fluids, particularly at the meso-scale.

Currently several diphasic LB-based methods exist, each employing a different algorithm to segregate the simulated fluids (see below). Here we attempt fundamentally to assess the *hydrodynamics* of a diphasic LB as it might be used to simulate multi-component flow: that is, in the narrow interface limit. Therefore, whilst the most recent segregation algorithms capture, for instance, phase separation kinetics,¹ for present purposes an adaptation² of a much earlier, minimal segregation algorithm due to Gunstensen³ is used. This algorithm is nevertheless capable of producing the narrow interfacial region germane to applications in multi-component flow simulation. Moreover the particular LB model is ancillary: our methodology might be applied to assess the hydrodynamics of any diphasic LB simulation.

Key developments in the monophasic LB method and its additional *segregation rules* for immiscible fluids are contained in refs. 1 and 3–12. Of all monophasic LB schemes, the simplest (Qian *et al.*,¹¹) is inspired by the work of Bhatnagar, Gross and Krook on the Boltzmann equation. The eponymous *lattice BGK* (LBGK) scheme designated D2Q9¹¹ is the *core* model for our diphasic LBGK, outlined in Section 2 (see also ref. 2). Diphasic lattice Boltzmann techniques allow one to calculate flows of immiscible fluid mixtures by augmenting the core lattice Boltzmann algorithm with an additional segregation rule which acts between the separated fluids, which are traditionally designated red and blue. These rules differ con-

siderably: in Shan and Chen,¹² Gunstensen *et al.*³ and Swift *et al.*¹ the interface is maintained in rather different ways and each of these extensions to the core LB method have been used to simulate a range of problems: Laplace Law behaviour,³ deformation and burst in droplets under shear in two dimensions,^{13,14} sheared phase separation in three dimensions and as a vehicle to study the kinetics of phase separation.^{1,15,16} The growing literature on the method has been reviewed by Rothman and Zaleski.¹⁷ Our particular model is defined in Section 2).

Broadly, the results from the different segregation algorithms are consistent with what is observed in the corresponding physical system. However, the extent to which any of the above methods are *hydrodynamic* at the meso-scale (in the sense that each should generate a surface of separation conforming with the boundary conditions obtaining at the deformable interface of tension between two viscous fluids¹⁸ has not, to our knowledge, been assessed. Researchers have, for example, measured diphasic LBs' interfacial properties macroscopically, by considering certain interfacial configurations (shapes), then comparing with known results from hydrodynamics: so the most direct measurements of a model's interfacial tension are from Laplace Law results applied to (assumed) circular drops, or from the pressure tensor definition of surface tension on planar interfaces, see for example refs. 3 and 13 and references therein. The meso-scale hydrodynamics of the interface remains uninvestigated.

We show here, for example, that Laplace Law behaviour emerges as an average from richer interfacial conditions. Moreover, we observe that a diphasic segregation algorithm in the narrow interface limit will tend to generate an anisotropic surface in consequence of the underlying lattice (see also ref. 2). This anisotropy does not preclude static Laplace law behaviour, or qualitatively correct hydrodynamics in respect of *e.g.*, sheared drop burst: interfacial behaviour is useful and passes a first macroscopic test. But issues of anisotropy in the surface tension, and the quality of the interfacial behaviour on the meso-scale are clearly relevant.

At their most general, the hydrodynamic boundary conditions for normal and tangential stress transmission, on the meso-scale at the isothermal interface between two immiscible fluids without gradients in the interfacial tension are:^{18,19}

$$\sigma_{\alpha\beta}^R n_\beta - \sigma_{\alpha\beta}^B n_\beta = \Sigma \left(\frac{1}{R_1} + \frac{1}{R_2} \right) n_\alpha \quad (1)$$

$$\sigma_{\alpha\beta}^R t_\beta - \sigma_{\alpha\beta}^B t_\beta = 0 \quad (2)$$

Here Σ is the macroscopic surface tension, $\sigma_{\alpha\beta}$ is the stress tensor, $\sigma'_{\alpha\beta}$ is the viscous stress tensor¹⁸ and the normal and tangent to the interface are represented by \hat{n} and \hat{t} respectively. R_1 and R_2 are the principle radii of curvature of the interface.¹⁸

The two dimensional Laplace law $\Sigma = \Delta p/R$ is a special case of eqn. (1) for zero flow. Whilst the Laplace law has been widely used to characterise multiphase LBGKs, we suggest that it is the extent to which the more general condition of eqn. (1) is represented in diphasic LBGK hydrodynamics that is the significant measure. Moreover eqn. (1) applies *locally*, to all interfacial elements in all cases (hence our designation *mesoscopic*) unlike the Laplace Law, which applies to a particular (zero-flow) situation. Indeed the correspondence between the surface tension known from static Laplace Law tests and that surface tension which governs the meso-scale dynamic response of the interface [in eqn. (1)] remains to be assessed in a direct investigation of the normal stress condition.

In any diphasic LBGK fluid, a closed narrow interface maintaining a pressure difference might well have properties different from a simple planar interface but those properties should depend only upon the local orientation of the interface with respect to the lattice and not (*e.g.*) upon the flow field or its derivatives. Thus a meso-scale surface tension, assessed through conditions eqns. (1) and (2) is, we suggest, the most significant interfacial parameter. The need for some reappraisal is further underlined by the results of previous study on macroscopic surface tension in our diphasic LBGK, reported in ref. 2 in which expressions for *pressure tensor* surface tension, for the two possible stable planar interface orientations, available to the lattice fluid in D2Q9 were derived. These expressions predict an anisotropy which is in good agreement with values measured from simulation and interface anisotropy and probably affects hydrodynamics on the mesoscale.

In this paper, then, we examine *with a generally applicable methodology* the extent to which general hydrodynamic conditions eqns. (1) and (2) are modelled by one particular derivative of the Gunstensen (Rothman–Keller) interface. As a by-product we indicate briefly some modifications which may improve the hydrodynamic properties of the Gunstensen-type diphasic LBGKs.

In Section we define our particular LBGK model, then (Section 3) examine, with a general method, the *tangential* properties of its interface, against the criterion of eqn. (2). Next we assess normal stress behaviour (Section 4).

Generally, in two dimensions, eqns. (1) and (2) may be re-phrased into a statement of interfacial hydrodynamics better suited to direct assessment (Section 4). Section 4 also contains an account of one means by which meso-scale measures of *any* LBGK interface may be made. That is, the investigative methods developed in Sections 3 and especially 4 apply to other LBGK interface generating techniques.^{12,14}

We present our conclusions in Section 5.

2 Model

Our model uses a core LBGK scheme on the square lattice designated D2Q9: Table 1 of ref. 2 defines its 9 velocities (c_i), $i = 1 \dots 9$ (links). The density at position x , time t is designated red or blue, and denoted $R_i(x, t)$, $B_i(x, t)$.

Multi-component behaviour arises as colour segregation is imposed by a generalisation of the core LBGK collision step¹¹ which re-allocates colour to the (net) link density $N_i(x, t) = R_i(x, t) + B_i(x, t)$, which is itself perturbed so as directly to insert anisotropy into the pressure tensor $P_{\alpha\beta}(x, t) = \Sigma_i N_i(x, t) c_{i\alpha} c_{i\beta}$.

We use an interface-generating perturbation modified from Gunstensen *et al.*³ which narrows the interface width, activating this surface tension generating perturbation only on sites occupied by two colours:²

$$\Delta N_i(x, t) = \sigma C(x, t) \cos[2(\theta_f - \theta_i)] \quad (3)$$

Here σ is the surface tension parameter controlling the perturbation amplitude, θ_i is the angular orientation of link identified in the subscript and $\theta_f(x, t)$ is the direction of a local colour gradient $f(x, t)$:

$$f(x, t) = \sum_{i,j} (R_j(x + c_i, t) - B_j(x + c_i, t)) c_i \quad (4)$$

and the factor $C(x, t)$ is a weighting concentration factor:

$$C(x, t) = 1 - \left| \frac{\rho_B(x, t) - \rho_R(x, t)}{\rho_B(x, t) + \rho_R(x, t)} \right| \quad (5)$$

the role of which is not without foundation in hydrodynamics^{2,20} and in parent lattice gas techniques.²¹ A fuller account of our particular interfacial perturbation is contained in ref. 2.

It is appropriate to comment that the interface created after the manner just discussed has, as one expects, a minimum “energy” when aligned parallel with lattice velocity vectors. Any modification to an interfacial perturbation with the general form of eqn. (3) is unlikely to influence this tendency, which is the most significant cause of anisotropy in this model’s interfacial tension.

3 Tangential stress condition

In this section we assess the tangential stress condition eqn (2) as it applies to our LBGK interfaces separating a blue/red/blue planar sandwich system (see Fig. 1) which is sheared in the the y -direction.

For this situation, hydrodynamics predicts a linear relation between shear stress and velocity gradient in the bulk of the separated fluids. Defining shear rate $\dot{\gamma}$ in the usual manner:

$$\frac{\partial u_y}{\partial z} = \dot{\gamma} \quad (6)$$

it is easy to show that, for separated, sheared blue and red fluids with different viscosities

$$\dot{\gamma}^R \nu^R = \dot{\gamma}^B \nu^B \quad (7)$$

where superscripts refer to the fluid colour in the obvious manner, symbol ν is fluid shear viscosity and $\dot{\gamma}$ the fluid shear

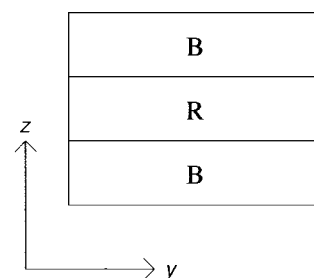


Fig. 1 Schematic of the lattice configuration for tangential stress examination. Periodic conditions were used to close all lattice boundaries, with horizontal forcing (Section 1.2) applied along sites in the lines at the top (bottom) of the top (bottom) blue layer.

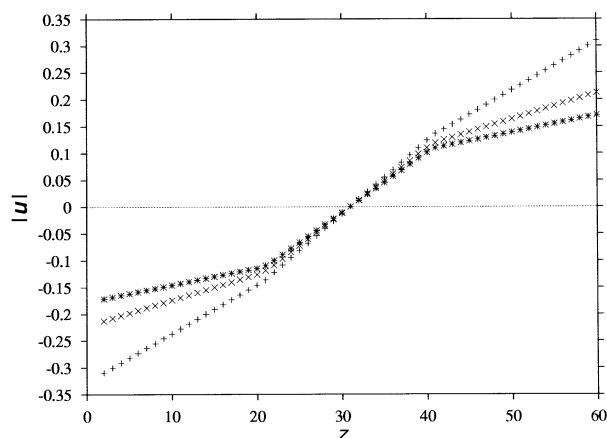


Fig. 2 Variation in y -averaged flow velocity $|u|$ against z for viscosity ratios of 1.5 : 1, 2.5 : 1 and 3.5 : 1.

rate. In addition to eqn. (7) the velocities of the separated red and blue components should match at the interface.

The transmission of tangential stress by our interface was assessed through eqn. (7), by examining the measured ratio between the separated fluids' different shear rates and comparing this with their set viscosities.

With periodic boundary conditions implemented in the y -direction a horizontal (shearing) flow was induced on the system of Fig. 1 by simply incrementing link densities to favour horizontal mass flux in opposite directions at the top and bottom of the lattice at each time step. This particular lattice-edge closure rule easily produces a lattice fluid shear rate controlled through the size to the forcing density increment (see *e.g.* ref. 22 for discussion).

The red/blue layers were set to different viscosities through the BGK relaxation parameter ω , the viscosity of mixed sites being controlled through an effective average relaxation parameter:

$$\omega_{\text{eff}} = \frac{\omega^R \rho^R + \omega^B \rho^B}{\rho^R + \rho^B} \quad (8)$$

At the shear rates used all our horizontal planar interfaces were observed to remain singular (one site thick). With a shear directed parallel to the interface, population of links by colour mass in the interfacial node was observed to be qualitatively similar with the static interfaces reported in ref. 2.

The sandwich system of Fig. 1 was evolved on a 90×60 lattice. Each layer was of approximately equal thickness. Layers were initialised with a viscosity ratio red : blue of 1.5 : 1, 2.5 : 1 and 3.5 : 1. The z -averaged shear rate was then measured in each horizontal fluid layer (in lattice units). Fig. 2, displays the result. It is important to note that the (fully) tangential velocity is clearly continuous across the interface, meeting the hydrodynamic condition of continuity of tangential velocity across an interface.

Separate fits to data from the red/blue layers established individual red/blue shear rates. These ratios correlate very well with the set ratios of red/blue fluid viscosity, as is clear from Table 1 which shows red/blue shear rate ratio against viscosity ratio. Regression to the data of Fig. 3 was found to

Table 1 Comparison of viscosity ratios with measured velocity gradient ratios

| Viscosity ratio | Velocity gradient ratio |
|-----------------|-------------------------|
| 1 : 1.5 | 1 : 1.505 |
| 1 : 2.5 | 1 : 2.513 |
| 1 : 3.5 | 1 : 3.522 |

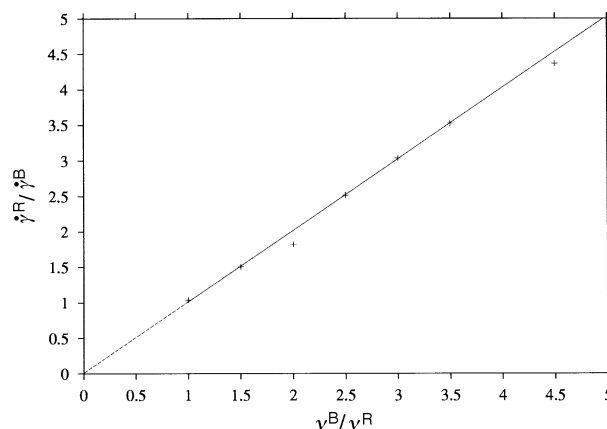


Fig. 3 Variation between $\dot{\gamma}^R/\dot{\gamma}^B$ against ν^B/ν^R .

lend good support to the expected relationship:

$$\dot{\gamma}^R/\dot{\gamma}^B = \nu^R/\nu^B \quad (9)$$

derived from eqn. (7). For the data in this study a surface tension parameter of $\sigma = 0.0125$ was used, with a shear forcing density increment of 0.02,²² the viscosity ranges were $\nu^R = 0.0294$ (corresponding to a relaxation parameter of $\omega^R = 1.7$) and $0.0140 \leq \nu^B \leq 0.1471$ ($1.1 \leq \omega^B \leq 1.7$).

Clearly, these results support the conclusion that tangential stresses are correctly handled by our LBGK interface. This observation assists the analysis of the normal stress behaviour, investigated in the next section.

4 Normal stress condition

Consider a red drop in the y - z plane surrounded by a blue fluid of equal density and viscosity, deformed by a flow, which in the blue far-field approximates to a shear. A point on the interface is specified by radial distance r and polar angle θ . In two dimensions the drop deformation may be characterised by a single local radius of curvature $R(\theta)$. The relevant quantities are represented in Fig. 4, in which the unit normal, \mathbf{n} , and (single) unit tangent, \mathbf{t} at the red/blue interface must be related through:

$$\hat{n}_y = -\hat{t}_z \quad \hat{n}_z = \hat{t}_y \quad (10)$$

When working in two dimensions it is possible to combine normal and tangential boundary conditions eqns. (1) and (2) into a more convenient form.

Using an obvious notation in which, *e.g.*, internal (red) velocity close to the interface is expressed v_α^R , the normal contraction of eqn. (1) may be written:

$$p^R - p^B + \sigma'_{\alpha\beta} n_\alpha n_\beta - \sigma_{\alpha\beta} n_\alpha n_\beta = \frac{\Sigma}{R(\theta)} \quad (11)$$

where we have used the relationship $\sigma_{\alpha\beta} = p\delta_{\alpha\beta} + \sigma'_{\alpha\beta}$ between stress and viscous stress.¹⁸ The analogous tangential contraction of eqn. (2) may be added to eqn. (11) and, on appeal to

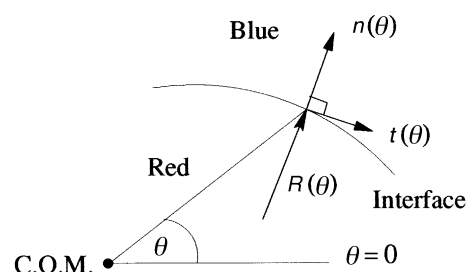


Fig. 4 Schematic of the unit normal and tangent vectors, drawn at a site on a discrete LBGK interface position characterised by angle θ . $R(\theta)$ represents the local radius of curvature of the interface.

the identities of eqn. (10), there results a modified statement of the normal stress condition, valid for two-dimensional situations:

$$p^R(\theta) - p^B(\theta) + 2\nu^R(\partial_y u_y^R + \partial_z u_z^R) - 2\nu^B(\partial_y u_y^B + \partial_z u_z^B) = \frac{\Sigma}{R(\theta)} \quad (12)$$

in which all derivatives and the hydrostatic pressures are evaluated approaching that interfacial location specified by the polar angle θ . Having already assumed incompressible flow, the separate divergences in eqn. (12) each vanish and for a two-dimensional fluid at the meso-scale:

$$\Delta p(\theta) = \frac{\Sigma}{R(\theta)}, \quad \Delta p(\theta) = p^R(\theta) - p^B(\theta) \quad (13)$$

in which, recall $R(\theta)$ is the *local* radius of curvature of the interface. So, in two dimensions the usual interfacial conditions are re-phrased into eqn. (13) and tangential stress eqn. (12). Looking back at eqn. (13) we can say that an LBGK model has “physical” hydrodynamics if the measured pressure difference divided by the local radius of curvature gives the same number at all interfacial positions θ .

The results of Section 3 clearly imply that tangential stress conditions eqn. (2) are met. To test the normal stress behaviour therefore, we can assess the extent to which diphasic LBGKs are described by eqn. (13).

From calculation on a flat interface, it has been shown that the surface tension of our particular diphasic LBGK varies with the interface's orientation relative to the underlying D2Q9 lattice.⁹ And in the narrow interface limit any diphasic LBGK's *meso-scale* interfacial hydrodynamics might be also be complicated by anisotropy. In applying eqn. (13) then, the factor Σ is assumed to have angular variation and we write:

$$\Delta p(\theta) = \frac{\Sigma(\theta)}{R(\theta)} \quad (14)$$

Note we propose eqn. (14) for 2D *only*, and then only when tangential stress continuity (Section 3) has been verified. Also, the angular variation of property $\Sigma(\theta)$ is an artifact of the particular model in use and of less interest than any method which may limit its amplitude. Indeed if $\Sigma(\theta)$ is made independent of θ , the hydrodynamics of the technique improves.

Further to assess any two-dimensional diphasic LBGK's hydrodynamics through compliance with eqn. (14), the pressure difference $\Delta p(\theta)$ and local radius of curvature $R(\theta)$ must be obtained for a general angular position θ on the interface (Fig. 4). Our examination of the transmission of normal stress across a red/blue interface therefore proceeds by describing the means by which radius of curvature and pressure jump measurements may be performed on the steady-state of a well-deformed drop.

4.1 Radius of curvature measurements

Take a red drop sheared to a steady-state deformation in a blue fluid (see ref. 22). To determine $R(\theta)$, the centre of red mass is first located from moments of red mass.²² The coordinates (y, z) of each interface (mixed colour) site, relative to the drop centre may then be used to calculate the polar angle θ subtended by the radius vector (Fig. 4). The interfacial unit normal vector \hat{n} at position θ can be calculated using a Frenet–Serret formula²³

$$\frac{d\hat{f}}{ds} = \kappa \hat{n} \quad (15)$$

where \hat{f} is the unit tangent vector, s is arc length and κ such that $\kappa^{-1} = R(\theta)$. From eqn. (15), the radius of curvature $R(\theta)$ can now be written in terms of the y and z components of the unit tangent:

$$\frac{1}{R(\theta)} = \left| \frac{d\hat{f}}{ds} \right| = \left[\left(\frac{d\hat{f}_y}{ds} \right)^2 + \left(\frac{d\hat{f}_z}{ds} \right)^2 \right]^{1/2} \quad (16)$$

in which the square bracket terms must now be written as θ -derivatives. Write

$$\begin{aligned} \frac{d\hat{f}}{ds} &= \frac{d\hat{f}}{d\theta} \frac{d\theta}{ds} \\ &= \frac{d}{d\theta} \frac{d\mathbf{r}}{ds} \left| \frac{d\mathbf{r}}{ds} \right|^{-1} \end{aligned} \quad (17)$$

where θ is the polar angle, and we have used the definition of the unit tangent \hat{f} :

$$\hat{f} = \frac{d\mathbf{r}}{ds} \quad (18)$$

Noting that:

$$\left| \frac{d\mathbf{r}}{d\theta} \right|^{-1} = \left[\left(\frac{dy}{d\theta} \right)^2 + \left(\frac{dz}{d\theta} \right)^2 \right]^{-1/2} \quad (19)$$

We may rewrite eqn. (17) using eqns. (18) and (19) as:

$$\begin{aligned} \frac{d\hat{f}}{ds} &= \left| \frac{d\mathbf{r}}{d\theta} \right|^{-1} \frac{d}{d\theta} \frac{d\mathbf{r}}{ds} \\ &= \left| \frac{d\mathbf{r}}{d\theta} \right|^{-1} \frac{d}{d\theta} \left[\frac{d\mathbf{r}}{d\theta} \left| \frac{d\mathbf{r}}{d\theta} \right|^{-1} \right] \end{aligned} \quad (20)$$

Performing the differentiations in eqn. (20) we obtain, for the y and z components of the unit tangent vector, at an interfacial location specified by θ

$$\frac{d\hat{f}_y}{ds} = \left| \frac{d\mathbf{r}}{d\theta} \right|^{-2} \left[\frac{d^2 y}{d\theta^2} - \frac{dy}{d\theta} \left| \frac{d\mathbf{r}}{d\theta} \right|^{-2} \left(\frac{d^2 y}{d\theta^2} \frac{dy}{d\theta} + \frac{d^2 z}{d\theta^2} \frac{dz}{d\theta} \right) \right] \quad (21)$$

$$\frac{d\hat{f}_z}{ds} = \left| \frac{d\mathbf{r}}{d\theta} \right|^{-2} \left[\frac{d^2 z}{d\theta^2} - \frac{dz}{d\theta} \left| \frac{d\mathbf{r}}{d\theta} \right|^{-2} \left(\frac{d^2 y}{d\theta^2} \frac{dy}{d\theta} + \frac{d^2 z}{d\theta^2} \frac{dz}{d\theta} \right) \right] \quad (22)$$

The local radius of curvature around a site specified by θ is thus obtained from eqn. (23) (reproduced below) using eqns. (21) and (22) (above) for the s -derivatives of the y and z components of the unit tangent.

$$\frac{1}{R(\theta)} = \left| \frac{d\hat{f}}{ds} \right| = \left[\left(\frac{d\hat{f}_y}{ds} \right)^2 + \left(\frac{d\hat{f}_z}{ds} \right)^2 \right]^{1/2} \quad (23)$$

To obtain approximations for the derivatives in eqn. (21), consider the interface site coordinates (y, z) to be functions of θ and write their respective Fourier sine/cosine series representations, each with period π :

$$y(\theta) \approx \frac{a_0}{2} + \sum_n [a_n \sin(n\theta) + b_n \cos(n\theta)] \quad (24)$$

$$z(\theta) \approx \frac{a'_0}{2} + \sum_n [a'_n \sin(n\theta) + b'_n \cos(n\theta)] \quad (25)$$

Clearly, derivatives like the $d^2 z/d\theta^2$ occurring in eqn. (21) may now be written explicitly in terms of a_0, a_n, a'_0, a'_n and b'_n and in turn Fourier amplitudes a_0, a_n and b_n etc. may be approx-

imated at given (measured) θ by numerical integration:

$$a_0 = \frac{1}{\pi} \int_{-\pi}^{\pi} y(\theta) d\theta \approx \frac{1}{\pi} \sum y(\theta_i) \Delta\theta_i \quad (26)$$

$$a_n = \frac{1}{\pi} \int_{-\pi}^{\pi} y(\theta) \sin(n\theta) d\theta \approx \frac{1}{\pi} \sum y(\theta_i) \sin(n\theta_i) \Delta\theta_i \quad (27)$$

$$b_n = \frac{1}{\pi} \int_{-\pi}^{\pi} y(\theta) \cos(n\theta) d\theta \approx \frac{1}{\pi} \sum y(\theta_i) \cos(n\theta_i) \Delta\theta_i \quad (28)$$

$$\Delta\theta_i = |\theta_i - \theta_{i-1}| \quad (29)$$

where $\Delta\theta_i$ is the (small but irregular) angular interval between neighbouring interfacial sites.

The local radius of curvature, at given θ was thus determined, from a fit to the whole drop interface using eqns. (21)–(23) with the appropriate derivatives obtained from the Fourier components given in (*e.g.*) eqn. (26). As a check, raw co-ordinates (y, z) were obtained from the Fourier components identified in eqn. (26). Fig. 5 displays results for a deformed drop (undeformed radius $R = 40$, $\sigma = 0.005$ and $\omega = 1.5$). By trial and error, fifteen Fourier harmonics ($n < 15$) were found to be sufficient to obtain good agreement between measured and interpolated interface positions.

Fig. 6 graphs the radius of curvature $R(\theta)$ measured for an undeformed drop, which, despite some asymmetry (attributable to the fact that the interface is narrow), exhibits periodicity (over intervals $-\pi \leq \theta \leq 0$ and $0 \leq \theta \leq \pi$). The mean value of the collected radius data gives a value of $\bar{R} = 40.236$.

4.2 Pressure ‘jump’ measurements

Fig. 7 plots pressure (density) and colour against horizontal distance from an undeformed drop centre. Clearly pressure oscillates close to a sharp colour interface, which oscillation, on the meso-scale, must be regarded as an artifact of a Gunstensen-type interface. Other diphasic LBGK algorithms also show variation in density across the interfacial region. What is essentially microscopic physics presenting at the mesoscale is an acknowledged aspect of LBGK simulation in general. Here, to measure a hydrodynamic pressure jump (in a way which will generalise to any diphasic LBGK) we measure

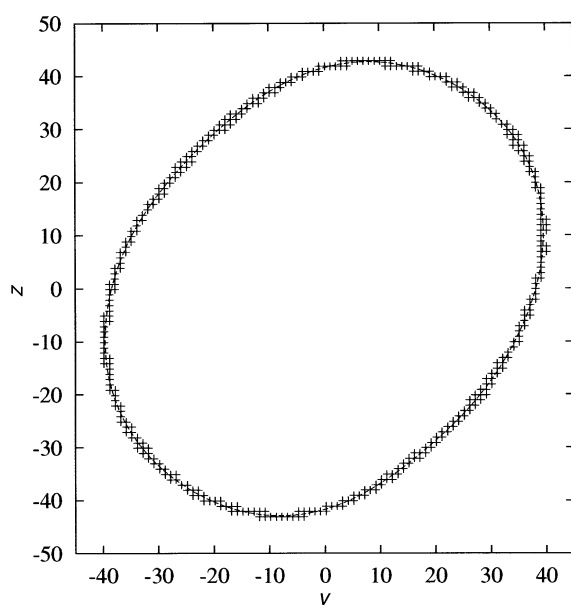


Fig. 5 Simulated interface data (+) for a sheared drop, superposed over the discrete Fourier fit to the interface for a drop with $R = 40$, $\sigma = 0.005$ and $\omega = 1.5$, (solid line).

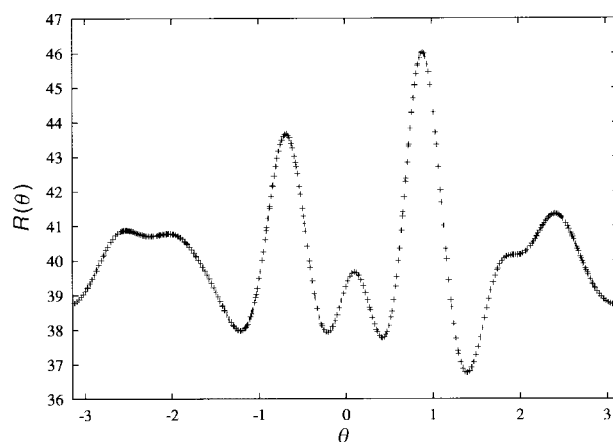


Fig. 6 Radius of curvature $R(\theta)$ against θ for the undeformed drop.

$\Delta p(\theta)$ between two points in the separated liquids which lie as close as possible to the colour interface, are characterised by the same θ , but which lie outside the region in which pressure is influenced by the particular segregation algorithm in use.

Shrinking/expanding the Fourier fit to the interface, by 5 lattice sites (a model-dependent number, small compared with simulation length scales, conditioned by the minimum simulated drop radius) one finds a pair of contours, concentric and locally parallel with the sharp colour interface. One point on each contour may be identified by a value of θ characterising some interfacial node. The two points inevitably lie off-lattice so interpolation between nodes was used to infer red (blue) pressure $p(R)$ [$p(B)$] and hence hydrostatic pressure jump at polar angle θ . Fig. 8 shows the variation of $p(R)$ and $p(B)$ with polar angle θ . Both sets of data show similar periodic fluctuations. The mean pressure outside the drop is $p \approx 0.6$ (local density $\rho/3$) resulting from an initial value $p = 1.8$. The data of Fig. 8 were extracted from a static drop on a 150×150 lattice with initial radius $R = 40$, $\omega = 1.5$ and interfacial $\sigma = 0.005$. Internal pressure data exhibits the flattest profile, and does not correlate to the drop radius of curvature as well as the external pressure variation.

4.3 Measurements of meso-scale surface tension

After the discussions of the last two sections we are now in a position to evaluate $R(\theta)$ and $\Delta p(\theta)$ for drops of any shape, and therefore obtain a meso-scale surface tension for our model from eqn. (14).

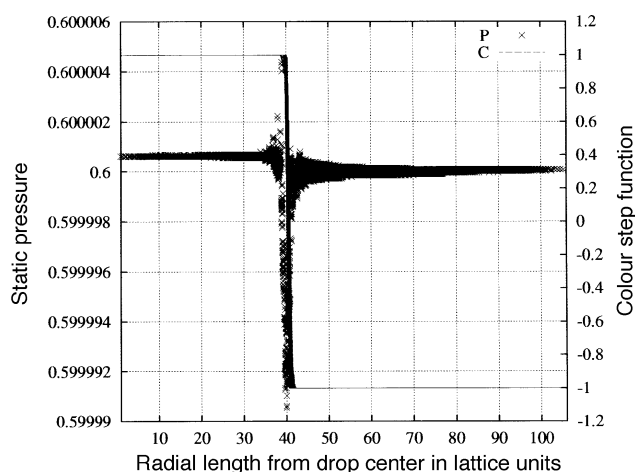


Fig. 7 Pressure and colour interface location as a function of normalised distance from the drop centre. Note that the colour interface is narrow (“singular”), whilst there is a clear oscillation in the pressure close to the interface, especially inside, in the red fluid.

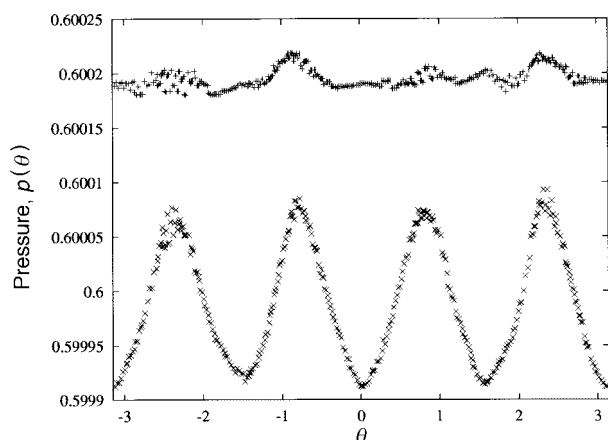


Fig. 8 Variation of static fluid pressure p with polar angle θ , inside the drop the symbol + is used.

Mesoscopic surface tension $\Sigma(\theta)$, when plotted against polar angle θ (Fig. 9: simulation details as in Fig. 8), has periodic structure consistent with the D2Q9 lattice and confirms that the mesoscopic surface tension $\Sigma(\theta)$, defined through eqn. (14) is anisotropic. With a minimum (maximum) value of $\Sigma(\theta)$, $\Sigma(\theta)_{\min} \approx 0.005$ ($\Sigma(\theta)_{\max} \approx 0.011$), the degree of surface tension anisotropy may be quantified by anisotropy factor:

$$A_\sigma = \frac{\Sigma(\theta)_{\max}}{\Sigma(\theta)_{\min}} \quad (30)$$

for the data of Fig. 9, $A_\sigma \approx 2.3$. Note, a single parameter such as A_σ cannot resolve all issues of interface anisotropy: there is in any sharp interface a tendency to adhere to lattice directions (observed in a correlation between measured surface tension and the direction of the interfacial tangent). However, whilst a close examination of the interface's constitution reveals it is mostly single site, its colour structure cannot be compared with that considered in ref. 2, which treats highly uniform, symmetric, *planar* interfaces with symmetric colour distribution and no density gradient or microcurrent.² Whilst the drop interface does tend to attach to the lattice (lying parallel to lattice directions) nowhere do we expect there to occur a zero pressure jump or a constant radius of curvature, so the variation observed in Fig. 9 is not covered by theory.²

A *standard* Laplace formula measurement of *macroscopic* surface tension is obtained from the mean static pressure inside the drop \bar{p}^R (over a radius of $r \leq 32$ lattice units from the drop centre), the external mean pressure \bar{p}^B (over nodes at radius $r \geq 48$: as is customary in the literature) and the radius of the drop (taken as the initialised radius of 40 lattice units)

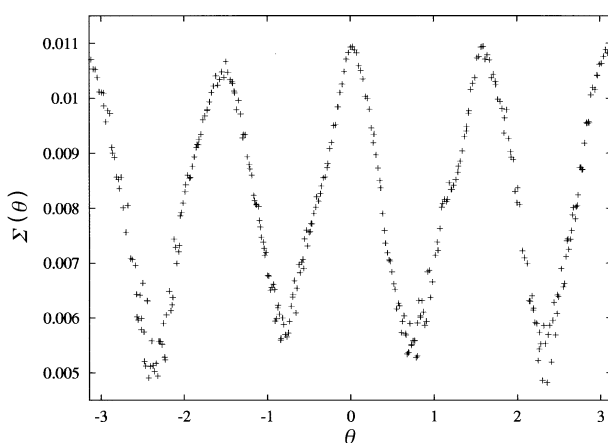


Fig. 9 Variation of macroscopic surface tension $\Sigma(\theta)$ with rotational angle θ .

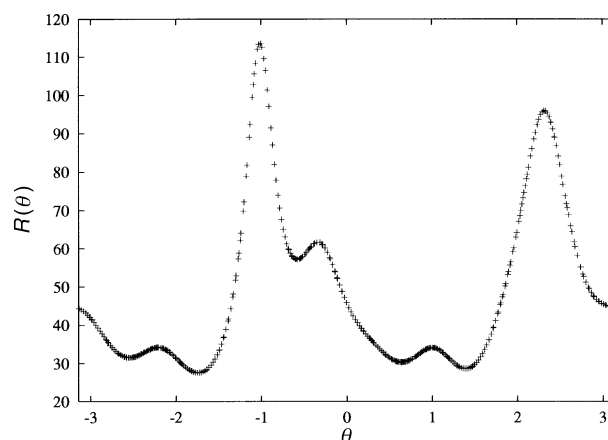


Fig. 10 Radius of curvature $R(\theta)$ against θ for the deformed drop of Fig. 5.

using:

$$\Sigma = R(p^{-R} - p^{-B}) \quad (31)$$

For the same drop, *standard* Laplace surface tension $\Sigma = 0.00772$ is recorded, the value of which is close to the mean mesoscopic surface tension, $\bar{\Sigma}(\theta) = 0.00797$, obtained from the data in Fig. 9. The usual Laplace Law surface tension is approximately the average of the local meso-scale surface tension data.

With a *deformed* (sheared) drop we notice strong local peaks in the radius of curvature (Fig. 10), corresponding with locations where the interface becomes tangent to lattice links, equivalent to a tendency of the interface to attach to D2Q9 lattice-link directions. With a narrow interface, curvature spikes are an artifact of the lattice: the former is inclined to align locally parallel with lattice link directions. Though the radius of curvature spikes are more apparent in the meso-scale data for a sheared drop, the underlying angular variation in surface tension (Fig. 11) is very similar to that obtained in static tests (Figs. 8 and 9).

Deformation changes the populations of different interfacial sites and the drop elongates along directions parallel to diagonal D2Q9 lines, with increasing applied shear. This process is clear from comparison of Figs. 9 and 11: equivalent stationary values of mesoscopic surface tension occur at angular positions θ which are slightly offset as a result of shape changes. For example, the same maximum value of mesoscopic surface tension occurs when the interface is parallel to the short links in the z -direction, around $\theta = 0$ rad in an undeformed drop

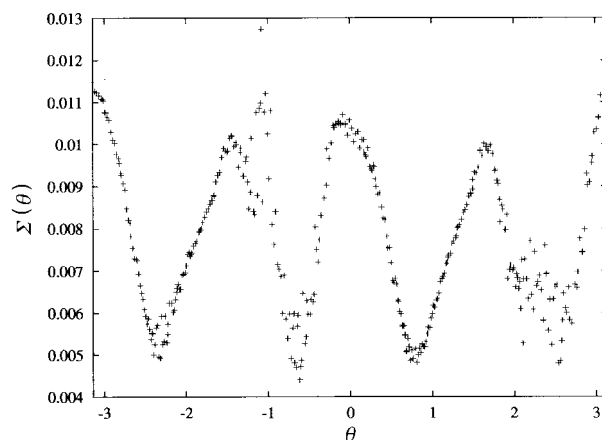


Fig. 11 Variation of macroscopic surface tension $\Sigma(\theta)$ with rotational angle θ for a deformed drop (corresponding radius of curvature data is in Fig. 10).

(Fig. 9) and around polar angle $\theta \approx -0.15$ rad (Fig. 11) in a deformed, sheared drop.

That the absolute shape of the drop does not influence the range of observed mesoscopic surface tensions or the interfacial orientations (relative to the lattice) at which the stationary values of surface tension are recorded leads us to the conclusion that, for our Gunstensen-type model, meso-scale surface tension anisotropy is primarily determined by local interfacial orientation, not by macroscopic detail (overall drop shape) and it should be possible to modify the mesoscopic surface tension behaviour using a *local* rule, that is, without recourse to details of the drop shape (*e.g.* radius of curvature).

Qualitatively then, static and deformed drops simulated using our diphasic LBGK model show a surface tension structure generally consistent with the lattice symmetry and “usual” macroscopic Laplace Law surface tension. Of course, for an LBGK interface to support hydrodynamical boundary conditions the meso-scale surface tension should produce flat profiles in Figs. 9 and 11. By modifying a model’s interfacial segregation rule one might improve the isotropy of meso-scale surface tension and hence make the LBGK model’s interfacial boundary conditions conform better with the defining eqns. (1) and (2).

Now, pressure tensor calculations appear to be a qualitatively correct description of the meso-scale surface tension of drops, so we write:²

$$\Sigma(\theta) \sim \frac{\sigma}{\omega} \quad (32)$$

where $\sigma(\omega)$ is the surface tension perturbation amplitude (LBGK relaxation parameter).

To improve meso-scale surface tension anisotropy in any LBGK model, one can vary σ to compete with the measured meso-scale interfacial tension. The detail of the following discussion depends upon the particular model of our study but the general methodology can be applied to any LBGK interface generating rule through its interface parameter.

Meso-scale surface tension should depend only upon the local interface orientation on the lattice. So taking the local colour field direction θ_f (or, in other models, the density gradient) to lie perpendicular to the local interface tangent, one can parametrise interface orientation on the lattice using θ_f , hence decrease $\Sigma(\theta)_{\max}$ and increase $\Sigma(\theta)_{\min}$ by contriving θ_f dependence in perturbation amplitude σ :

$$\Delta N_i(\mathbf{x}, t) = \sigma g(\theta_f) C(\mathbf{x}, t) \cos[2(\theta_f(\mathbf{x}) - \theta_i)] \quad (33)$$

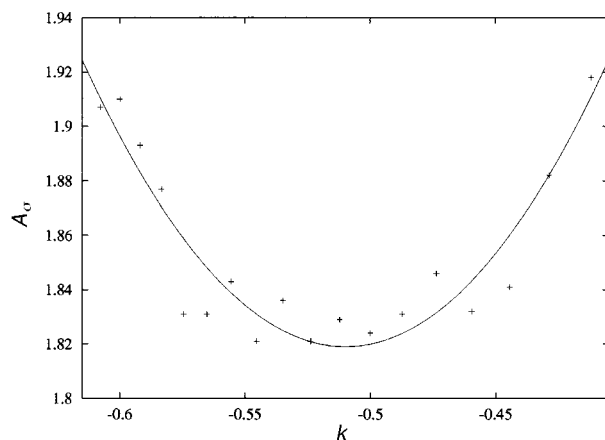


Fig. 12 Variation of drop anisotropy factor A_σ with parameter k , close to the minimum in A_σ . The continuous line fit has the form $ax^2 + bx + c$ for $a = 9.525$, $b = 9.714$ and $c = 4.296$. Outside the range shown anisotropy increases monotonically.

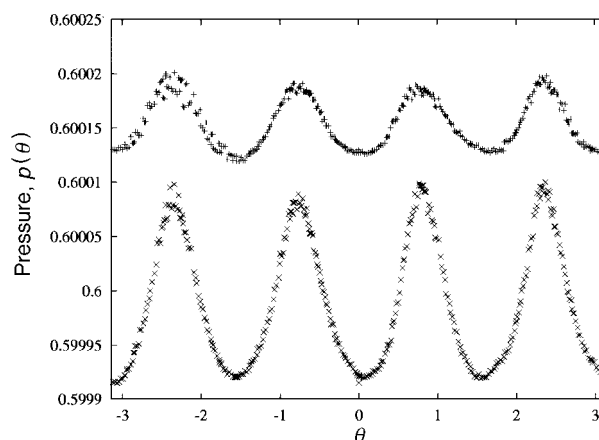


Fig. 13 Variation of static fluid pressure p with rotational angle θ , close to the interface (but see Fig. 8).

where factor $g(\theta_f) = g(\theta_f + \pi/2)$ promotes surface tension isotropy. For our particular interface we may choose

$$g(\theta_f) = \{1 + k \cos^2[2\theta_f(\mathbf{x})]\} \quad (34)$$

in which k is a real parameter $-1 \leq k \leq 0$ (see Figs. 10 and 11) which may be optimised by considering undeformed drops, for which $\theta_f \approx \theta$, the polar angle of an interfacial length element. Considering eqns. (33) and (34):

$$\Sigma(\theta)' \approx g(\theta) \Sigma(\theta) \quad (35)$$

where $\Sigma(\theta)'$ [$\Sigma(\theta)$] is the meso-scale surface tension, at polar angle θ from the modified (original) model. From Fig. 9 $\Sigma(\theta)_{\max} = \Sigma(0)$, $\Sigma(\theta)_{\min} = \Sigma(\pi/4)$ so stating interfacial isotropy as $\Sigma(0)' = \Sigma(\pi/4)'$ use eqn. (35) and definition eqn. (34) to obtain:

$$A_\sigma = \frac{g(\pi/4)}{g(0)} = \frac{1}{1+k} \quad (36)$$

where we have used *e.g.* $g(0) = 1 + k$. Using a measured value of 2.3 for A_σ we estimate $k = -0.52$, which is supported by simulation (Fig. 12). Comparing Figs. 13 and 8, we note better correlation between pressures on the red and blue sides of our interface, which acts qualitatively to adjust interfacial tension as desired. But the radius of curvature has an essentially unchanged angular variation (from Fig. 10) so Fig. 13 shows only limited reduction of the amplitude of the variation of surface tension, compared with the unmodified algorithm (Fig. 9). Figs. 12–14 were obtained for an undeformed drop of initial radius $R = 40$ on lattices of edge 150×150 with $\sigma = 0.005$ and $\omega = 1.5$.

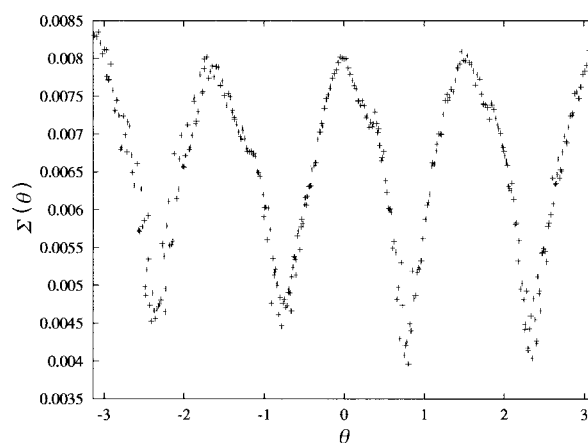


Fig. 14 Variation of macroscopic surface tension $\Sigma(\theta)$ with rotational angle θ .

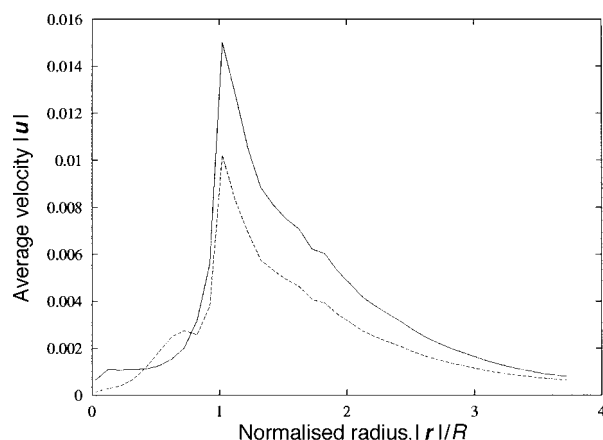


Fig. 15 Variation of $|u|$, microcurrent flow speed measured in units of lattice spacing per time step, against normalised distance from the drop centre, $|r|/R$ at $\sigma = 0.005$ for the unmodified interface (solid line) and the modified interface (broken line) at $k = -0.524$

Fig. 15 shows the spatial variation of microcurrent speed, $|u|$ for our steady-state drop. The solid line shows the angular-averaged magnitude of microcurrent velocity using the unmodified interface perturbation, the broken line with lower maxima shows the magnitude of microcurrent activity using the new algorithm at $k = -0.52$. Comparisons between microcurrents induced in Gunstensen–Rothman–Keller derivative and *e.g.* Shan–Chen interfaces²⁴ show $|u|_{\max}$ is twice as large in the former for similar interface perturbation parameters σ .²⁵ However a similar process of calibration on a Shan–Chen type model should be straightforward, and would enable that model further to reduce microcurrent intensity.

5 Conclusions

Using as a vehicle a minimalist segregation algorithm, after Gunstensen *et al.*,³ implemented over a D2Q9 LBGK algorithm, we have highlighted the need *locally* to evaluate the surface tension in any diphasic LBGK, used in the limit of narrow interfaces for simulations in which interfacial hydrodynamics is important.

To assist an analysis we have developed the means by which the general hydrodynamics of the interface may be quantified in two-dimensional LBGK simulations and we have presented a method by which the parameters [local interfacial curvature, pressure difference (see below)] may be obtained for discrete models. From this platform we have measured, at the meso-scale, the anisotropy inherent in our class of LBGK interface from a consideration of stresses across the interface.

Assessing the transmission of tangential stresses across planar interfaces in our LBGK model, *via* simulation measurements of the relationship between the separated fluid shear rates and viscosities, we obtain good hydrodynamics (velocity and stress continuity). The examination of normal stress transmission was supported by a Fourier interface investigation technique developed in Section 4, which is quite general in two dimensions and makes no assumptions about the shape of the fluid drop.

We illustrate how a simple modification to an interfacial algorithm can be used to improve interface properties [eqn. (34)] by adding a compensating oscillation in the interfacial parameter which makes a drop's internal and external pressures correlate with local interface orientation relative to the lattice. But unlike pressure, the interface's local radius of curvature is, we suggest, influenced by the tendency of the interface to adhere to lattice directions, which is probably

inevitable in any narrow interface. A diphasic LBGK density perturbation can, on general grounds, do little to adjust this. However we do produce a reduction in the magnitude of the microcurrent.

The local radius of curvature measurement in Fig. 10 is dominated by the interface's tendency to adhere to the lattice. Probably it represents the best attainable (most isotropic) radius of curvature variation for a drop resolved on a D2Q9 lattice as Fig. 10 was found to contain similar structure to an initialised *unevolved* drop: Fig. 10 shows how circular a single-site interface drop can be made on the lattice. Pressure differences do not appear to drive radius of curvature and we suggest that the interface in all classes of LBGK interface (and thereby radius of curvature) needs to be liberated from the lattice to allow the shape of the interface, as it were, more scope to adapt to local flow conditions. One means to achieve this might be to ensure that the colour field always lies normal to interface *i.e.* that the interface always lies perpendicular to the local colour gradient and that the segregating colour fluxes always direct along the colour field (in the present model segregating colour is allocated according to a tractable rule which does not ensure that the flux lies perpendicular to the interface).

References

- 1 M. R. Swift, W. R. Osborn and J. M. Yeomans, *Phys. Rev. Lett.*, 1995, **75**, 830.
- 2 I. Halliday, C. M. Care and S. P. Thompson, *Phys. Rev. E*, 1998, **57**(1), 514.
- 3 A. K. Gunstensen, D. H. Rothman, S. Zaleski and G. Zanetti, *Phys. Rev. A*, 1991, **43**(8), 4320.
- 4 U. Frisch, D. d'Humieres, B. Hasslacher, P. Lallemand, Y. Pomeau and J. P. Rivet, *Complex Syst.*, 1987, **1**, 649 and references therein.
- 5 R. Benzi, S. Succi and M. Vergassola, *Phys. Rep.*, 1992, **22**(3), 145.
- 6 Y. H. Qian, S. Succi and S. A. Orszag, *Annu. Rev. Comput. Phys.*, 1995, **3**, 195.
- 7 H. Chen, S. Chen and W. H. Matthaeus, *Phys. Rev. A*, 1992, **45**(8), R5339.
- 8 D. d'Humieres, P. Lallemand and U. Frisch, *Europhys. Lett.*, 1986, **56**, 1505.
- 9 F. Higuera and J. Jimenez, *Europhys. Lett.*, 1989, **9**, 7, 663.
- 10 F. Higuera, S. Succi and R. Benzi, *Europhys. Lett.*, 1989, **9**(4), 345.
- 11 Y. H. Qian, D. d'Humieres and P. Lallemand, *Europhys. Lett.*, 1992, **17**(6), 479.
- 12 X. W. Shan and H. D. Chen, *Phys. Rev. E*, 1994, **49**(4), 2941.
- 13 I. Halliday and C. M. Care, S. Thompson and D. White, *Phys. Rev. E*, 1996, **54**(3), 2573.
- 14 A. J. Wagner and J. M. Yeomans, *J. Mod. Phys. C*, 1997, **8**(4), 773.
- 15 E. Orlandini, M. R. Swift and J. M. Yeomans, *Europhys. Lett.*, 1995, **32**, 463.
- 16 E. Orlandini, G. Gonnella and J. M. Yeomans, *Physica A*, 1997, **240**(1–2), 277.
- 17 D. H. Rothman and S. Zaleski, *Rev. Mod. Phys.*, 1994, **52**, 1417.
- 18 L. D. Landau and E. M. Lifshitz, *Fluid Mechanics*, Pergamon Press, Oxford, UK, 1966.
- 19 G. K. Batchelor, *An Introduction to Fluid Mechanics*, Cambridge University Press, Cambridge, UK, 1973.
- 20 J. S. Rawlinson and B. Widom, *Molecular Theory of Capillarity*, Oxford University Press, London, UK, 1989.
- 21 D. H. Rothman and J. M. Keller, *J. Stat. Phys.*, 1988, **52**(3–4), 1119.
- 22 I. Halliday and C. M. Care, *Phys. Rev. E*, 1995, **53**(3), 1602.
- 23 M. R. Spiegel, *Vector analysis and an introduction to Tensor analysis, Schaum's Outline Series*, McGraw-Hill, New York, USA, 1959.
- 24 S. Chen, G. D. Doolen, K. Eggert, D. Grunau and Y. E. Loh, *Phys. Rev. A*, 1994, **43**(12), 7053.
- 25 S. Hou, X. Shan, Q. Zou, G. D. Doolen and W. E. Soll, *J. Comput. Phys.*, 1997, **138**(2), 695.